
DATA-DRIVEN UNCERTAINTY-AWARE FORECASTING OF SEA ICE CONDITIONS IN THE GULF OF OB BASED ON SATELLITE RADAR IMAGERY

Stefan Maria Ailuro^{1,2,*}, Anna Nedorubova¹, Timofey Grigoryev¹, Evgeny Burnaev^{1,3}, Vladimir Vanovskiy^{1,2}

¹Applied AI Center, Skolkovo Institute of Science and Technology, Moscow, Russia

²Moscow Institute of Physics and Technology, Dolgoprudny, Russia

³Autonomous Non-Profit Organization Artificial Intelligence Research Institute (AIRI), Moscow, Russia
{sm.ailuro, a.nedorubova, t.grigorev, e.burnaev, v.vanovskiy}@skoltech.ru

ABSTRACT

The increase in Arctic marine activity due to rapid warming and significant sea ice loss necessitates highly reliable, short-term sea ice forecasts to ensure maritime safety and operational efficiency. In this work, we present a novel data-driven approach for sea ice condition forecasting in the Gulf of Ob, leveraging sequences of radar images from Sentinel-1, weather observations, and GLORYS forecasts. Our approach integrates advanced video prediction models, originally developed for vision tasks, with domain-specific data preprocessing and augmentation techniques tailored to the unique challenges of Arctic sea ice dynamics. Central to our methodology is the use of uncertainty quantification to assess the reliability of predictions, ensuring robust decision-making in safety-critical applications. Furthermore, we propose a confidence-based model mixture mechanism that enhances forecast accuracy and model robustness, crucial for reliable operations in volatile Arctic environments. Our results demonstrate substantial improvements over baseline approaches, underscoring the importance of uncertainty quantification and specialized data handling for effective and safe operations and reliable forecasting.

Keywords: Arctic Sea Ice Forecasting · Satellite Radar Imagery · Ensemble Forecasting · Uncertainty Quantification · Machine Learning for Video Prediction

Introduction

Problem statement

The Arctic region is experiencing an unprecedented rate of warming, leading to a significant reduction in sea ice area by more than 30% over the last four decades, and a simultaneous decrease in sea ice thickness [1]. Alongside this, the last century has seen active development of icebreaker construction technologies, including nuclear-powered ones. These changes have opened up new sea routes, such as the Northern Sea Route, which provide faster and more economical transport. However, increased navigation is accompanied by increased risks due to ice jams, posing a serious threat to maritime safety.

Traditional sea ice models, based on elastic-visco-plastic rheological properties, often fail to accurately reflect all the nuances of ice deformation, rendering them unreliable for forecasting in some cases [2, 3, 4, 5]. Additionally, these models require significant computational resources to adequately simulate the interactions between the ocean and ice. Consequently, there is a need to explore alternative methodologies that leverage statistical methods such as machine learning techniques, known for their flexibility and lower computational demands.

*Correspondence: ailuro.sm@gmail.com

Our research is aimed at improving the forecasting of ice conditions in the Gulf of Ob, a region significantly influenced by the interaction of the saline waters of the Kara Sea and the fresh water of the big northern rivers, leading to complex ice formation dynamics [6, 7].

We utilize radar images obtained in the Sentinel-1 mission [8], weather observation data [9], and operational forecasts and reanalysis from the GLORYS project [10] to predict future sea ice conditions. From a machine learning perspective, the series of satellite radar images can be treated as a continuous video sequence, therefore the problem can be formulated as a conditioned video prediction task — the widely investigated problem in common-life domain [11]. Our research employs advanced video prediction models, which include:

- Implicit Stacked Autoregressive Model for Video Prediction (IAM4VP)[12] uses a fully convolutional neural network with an implicit multi-input-single-output workflow, achieving state-of-the-art accuracy of weather predictions in datasets such as SEVIR;
- Dynamic Multi-Scale Voxel Flow Network (DMVFN) [13] utilizes voxel flow for video prediction, addressing efficiency and adaptability in handling diverse motion scales;
- MotionRNN [14] models spacetime-varying motions using the Motion Gating Recurrent Unit and Motion Highway mechanisms, enhancing prediction accuracy in dynamic scenarios;
- Neural Ordinary Differential Equations (Neural ODE) and Vid-ODE [15] treat consecutive frames as solutions to systems of ordinary differential equations, offering control over visual attributes and smooth transitions between frames.

As the primary loss for training models and metric for evaluating their performance, we use Mean Squared Error (MSE) between predicted and target Synthetic-Aperture Radar (SAR) images. In addition to this, we utilize the Structural Similarity Index (SSIM)[16] and its extension, the Multi-Scale Structural Similarity Index (MS-SSIM)[17], to assess the perceived quality of digital images and videos. Finally, the Integrated Ice Edge Error at level c (IEEE@c)[18] is utilized to measure the similarity between forecasted and observed ice sheets. These indicators allow us to meticulously compare the accuracy of predicted ice conditions against observed data, ensuring that our models reflect not only general trends but also detailed spatial structures necessary for accurate ice mapping.

Our contributions can be summarized as follows:

- we explore the potential of modern deep learning video-prediction models in short-term regional sea ice forecasting;
- we address the problem of data irregularity and missing values within the Arctic area by exploring filtration, normalization, and augmentations techniques;
- we propose an ensemble based approach for uncertainty quantification and suggest the confidence-based model selection scheme that enhances metrics and stabilizes the forecast;
- finally, we assess a gap filling performance for satellite radar imagery and demonstrate the superiority of our method in comparison with a general approach for interpolating video sequences.

Related works

Several studies have demonstrated the effectiveness of machine learning in forecasting sea ice extent and sea ice concentration. Chi and Kim [19] pioneered in the use of deep learning for sea ice prediction. Their model employs multilayer perceptrons (MLPs) and long- and short-term memory networks (LSTMs) to capture complex relationships in sea ice data. By training the MLP- and LSTM-based models on historical data, they identify patterns for one-month predictions, outperforming traditional statistical models. This work highlights the advantages of deep learning in sea ice forecasting.

Zhang et al. [4] introduced a framework that combines machine learning with causal analysis for short-term prediction of sea ice concentration. Their framework employs different machine learning algorithms, namely self-adaptive differential extreme learning machine, random forest, classification and regression tree, and support vector regression, to identify the most influential environmental factors. Through causal analysis, they select the most relevant variables, improving prediction accuracy and interpretability. This work emphasizes the importance of understanding the fundamental relationships between sea ice and its environmental drivers.

Recent research has extended the application of UNet-based models to sea ice forecasting, highlighting their versatility beyond original medical imaging applications. Fernandez et al. [20] investigated coastal sea elements forecasting using various UNet-based architectures, including 3DDR-UNet and its enhanced versions. Their study demonstrated the effectiveness of these models in forecasting coastal sea conditions when using satellite imagery. Grigoryev et al. [21]

presented a recurrent UNet with a specialized training scheme that considerably outperformed persistence and linear trend baseline forecasts of sea-ice conditions in the regions of the Barents, Labrador, and Laptev seas for lead times up to 10 days. Kvanum et al. [22] showed that the similar approach in the Barents sea can overcome traditional numerical models at the forecasting of sea ice concentration at one kilometer resolution and 3-day lead time. Keller et al. [23] explored various UNet-based architectures for prediction sea ice extent at kilometer resolution for lead time up to 7 days. These studies revealed the potential of machine learning methods over traditional approaches for high-resolution sea ice conditions forecasting.

Several studies showcase the prospects of uncertainty-aware data-driven sea ice forecasting. Horvath et al. [24] suggested using Bayesian logistic regression to forecast September minimum ice cover from 1-month up to 7-month lead times. In this paper Bayesian uncertainty quantification helps to assess the reliability of the forecasts. Andersson et al. [25] introduced a probabilistic deep learning sea ice forecasting system called IceNet with 6-month lead time. Their system predicts monthly averaged sea ice concentration maps at 25-km resolution, outperforming traditional models by effectively bounding the ice edge. Wu et al. [26] suggested VAE-Based Non-Autoregressive Transformer for long-term sea ice concentration forecast along Northern Sea Route. Variational autoencoder in its architecture provides the confidence estimation. Also uncertainty quantification is the key motive of the conjugate problems like sea ice data assimilation [27] or sea ice concentration retrieval [28].

One challenge in sea ice forecasting and analysis based on satellite imagery data is the presence of noise and gaps, which can occur due to instrumental errors, data losses, and environmental factors. To address this, researchers have proposed various gap-filling methods [29]. They incorporate chained data fusion, multivariate interpolation, and empirical orthogonal functions to effectively fill missing data. Weiss et al. [30] proposed an effective approach for continental-scale gaps inpainting based on nearest neighbors method and taking in account seasonality of the data. Their approach, additionally, quantified uncertainty of the filled values. Appel [31] introduced a deep learning approach based on partial convolutions for filling gaps in consecutive data, highlighting the promise of deep learning for satellite imagery-related tasks. These methods enhance the quality and reliability of remote observations, having potentially a wider range of applications than just sea ice analysis.

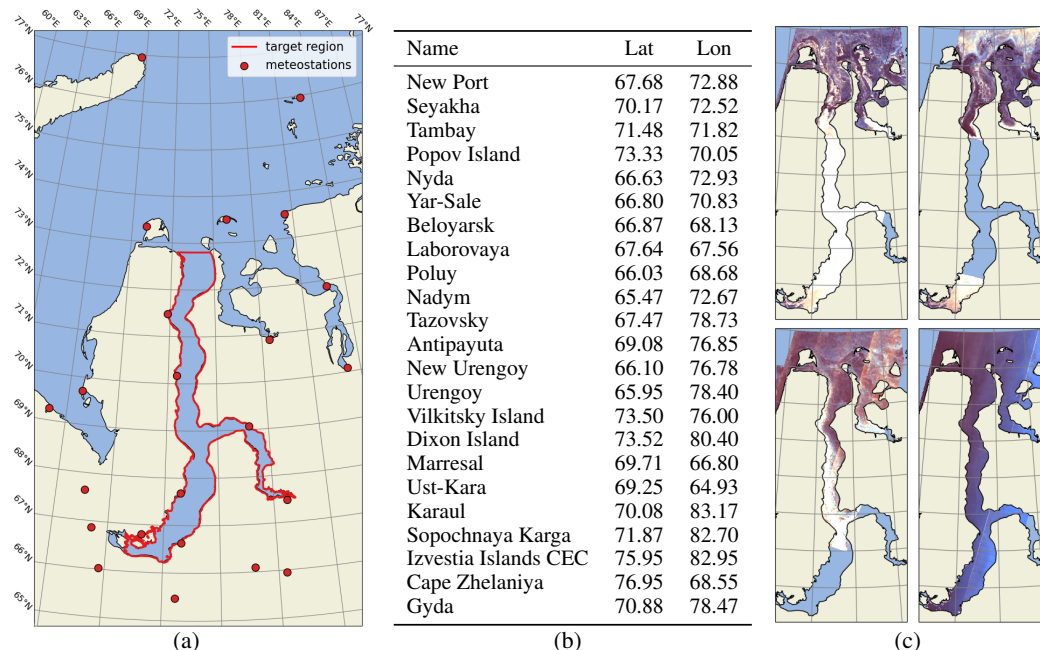


Figure 1: The map (a) and coordinates (b) of meteorological stations used, along with the target region outlined in red. Available sea surface area is 120,559 km². The area of interest is 51,262 km². (c) Examples of colorized SAR images

Data

Target region

The region we investigated encompasses the Gulf of Ob and the Taz Estuary in Northern Russia (see Figure 1). The Gulf of Ob, located at the mouth of the Ob River in the Arctic Ocean, is the world’s longest estuary, stretching approximately 1,000 km between the Gyda and Yamal peninsulas [32]. It is relatively shallow, with depths averaging 10 to 12 meters, limiting heavy sea transport.

The Taz Estuary, formed by the Taz River, spans about 330 km from Tazovsky to the Gulf of Ob, with an average width of 25 km. It flows north to south and then bends westward before merging with the Gulf of Ob, contributing to one of the largest estuarine systems in the world.

This region is important for sea ice forecasting and research due to its highly variable ice conditions influenced by seasonal changes and river discharge [7]. It’s a sensitive indicator of climate change and has significant economic and strategic value due to its location near major shipping routes and natural resources [33]. The unique interaction between river outflows and the sea creates distinctive ice patterns, making it a key area for studying sea ice dynamics and improving predictive models[34]. Additionally, sea ice in this region affects local ecosystems and communities, highlighting the broader impacts of environmental changes on ecology and society.

Input fields

Our neural network model utilizes a number of input channels (fields) that come from three sources: Sentinel-1[8], Global Ocean Physics Reanalysis (GLORYS)[10], and historical data from meteostations[9] (see Figure 1 for detailed information). Sentinel-1 SAR images and GLORYS fields are interpolated bilinearly to match the input resolution (1 km), data from meteostations is interpolated between discrete points (where the meteostations are located) using RBF interpolation method with thin plate splines [35]. The details on resulting channels and preprocessing for input data are described in Table 1.

Source	Scale	Channel	Normalization
Sentinel-1	1 km	SAR HV	$U(0, 1)$
		SAR HH	$U(0, 1)$
GLORYS	5 km	Bottom Temperature	$U(-1, 1)$
		Mixed Layer Thickness	$U(-1, 1)$
		Surface Salinity	$U(-1, 1)$
		Surface Temperature	$U(-1, 1)$
		Sea Ice Velocity (u)	$N(0, 1)$
		Sea Ice Velocity (v)	$N(0, 1)$
		Sea Height	$N(0, 1)$
Meteostations	-	Relative Humidity	$U(0, 1)$
		Air Pressure	$N(0, 1)$
		Air Temperature	$N(0, 1)$
		Wind Velocity (u)	$N(0, 1)$
		Wind Velocity (v)	$N(0, 1)$

Table 1: Description of input channels. GLORYS channels are interpolated bilinearly. Meteodata are interpolated using radial basis function interpolation.

Format of the forecasts

In this study we selected Sentinel-1 SAR imagery [8] as one of the inputs for the model and a target presentation of the forecasts, due to several key advantages it offers. Firstly, the all-weather capability of Sentinel-1 allows for continuous monitoring of polar regions regardless of cloud cover or illumination. The data consistency and reliability of Sentinel-1, coupled with its high revisit frequency, ensures a stable and reliable data stream for monitoring dynamic sea ice conditions and short-term forecasting. Secondly, the high spatial resolution of Sentinel-1 (up to 50 meters) enables detailed analysis of sea ice, including the detection of small-scale ice features important for navigation and environmental monitoring. Thirdly, the large amount of historical data provided by Sentinel-1 is essential for training deep learning models. Finally, the almost real-time data delivery of Sentinel-1 is crucial for operational applications.

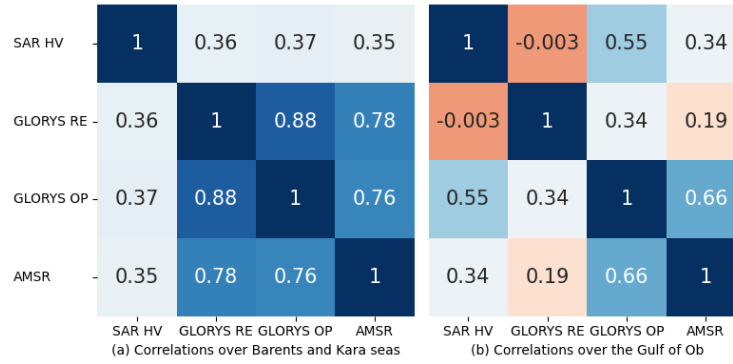


Figure 2: Mean cell-wise sea ice concentration correlation between several data sources: Sentinel-1 SAR [8], GLORYS operative and reanalysis [10], and AMSR [36]

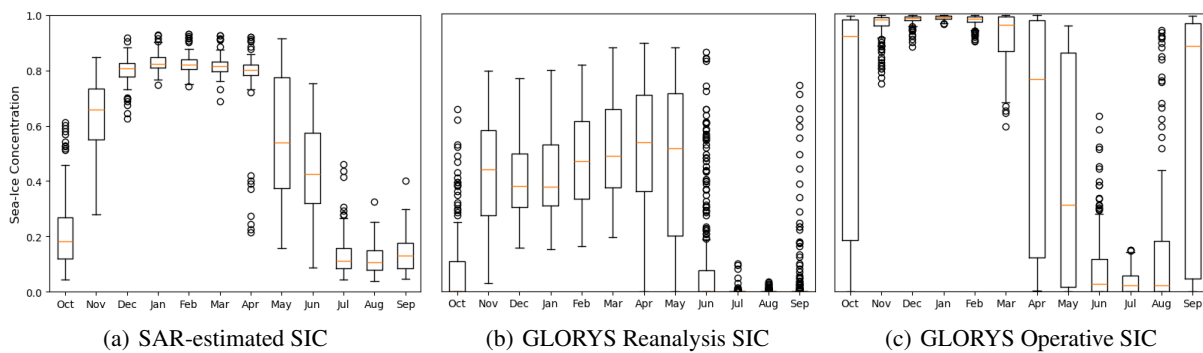


Figure 3: Box and whisker plots of SIC data distribution in the region in GLORYS and Estimated from SAR-images for different months from all available range of time, aggregated over target region. The box extends from the 25th percentile to the 75th percentile; whiskers extend the box by 1.5x of its length. The orange line is the median (50th percentile); SAR-estimated SIC is a normalized mean absolute value of SAR signal with dropped frames with more than 50% missing values.

In comparison to other potential target variables, such as GLORYS reanalysis, which lacks quality of ice data in the Gulf being mostly uncorrelated with other sources (see Figure 3), GLORYS operative analysis and forecasts, which lack historical records essential for data-driven approaches, and AMSR [36], which is partly dependent on cloud conditions and seasons, Sentinel-1 SAR imagery emerges as a superior choice for high-resolution sea ice forecasting models.

While the direct comparison between SAR and calculated sea ice concentrations is not strictly fair, the techniques of retrieval and mapping sea ice conditions from SAR imagery are well-known. Sentinel-1 C band consists of four polarizations, for the purpose of forecasting ice conditions we utilize colorized HV polarization [37]. Figure 2 shows the comparison of monthly-averaged sea ice concentrations from several sources.

Sentinel-1 SAR imagery has a great potential for forecasting up to tens of meters resolution, however it is computationally costly to fully cover the target region. Moreover, deep learning models require fine architectural tuning [38] to operate on high-resolution ($\geq 1K$) images. For the purpose of this study we set the target resolution to one kilometer, which nevertheless is sufficient enough for navigation applications [22, 23]. The region of interest, at this resolution, produces images with a size of 880×400 pixels. SAR images are interpolated conservatively to a covering equal-area grid in North-Polar projection (depicted on Figure ??). To focus on forecasting sea-ice dynamics, the land surface is masked with zero values.

When analyzing satellite images of our area of interest, we found several artifacts that significantly complicate processing. Firstly, the study area is not always imaged daily, causing many empty frames to appear when attempting to create a regular time series sequence. Secondly, the entire area is not always captured in the images, resulting in some images being incomplete. Thirdly, thermal noise and imagery artifacts at selected polarization are significant, leading to varying brightness in repetitive patterns known as scalloping.

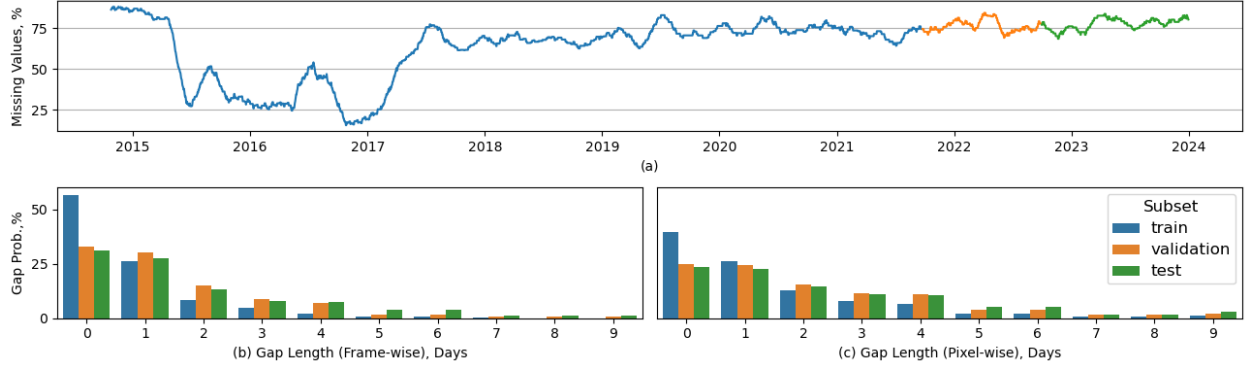


Figure 4: (a) Frequency of missing values in SAR imagery smoothed with a month-wide rolling window. (b-c) Distribution of distances between consecutive missing values across all subsets, calculated frame-wise between frames with any valid data, and pixel-wise at fixed locations.

Data split

The data is divided into three sets as follows:

- Training set: September 1, 2015, to September 23, 2021.
- Validation set: September 24, 2021, to September 30, 2022;
- Test set: October 1, 2022, to September 30, 2023;

The distribution of missing values over subsets is depicted in Figure 4.

Methods

Data preprocessing and filtration

The origin of the noise in SAR imagery is thermal interference within radar systems, influenced by the technology utilized for surface scanning, resulting in presence of speckles and scalloping patterns [39]. Thermal artifacts have significant magnitude relative to useful information, which leads to huge biases and corrupts optimization convergence of neural networks. Therefore, we preprocess data to filter out imagery artifacts. The results of the final filtering are presented in Figure 5.

Our custom filtering algorithm treats images as vectors from $\mathbb{R}^{H \times W}$ space with standard scalar product, where H and W stand for sizes of the input frames. The core assumption is the orthogonality of artifacts A to the subspace of clear images $C \perp A$. Therefore, the filtering process is an orthogonal projection: $P : \mathbb{R}^{H \times W} \rightarrow C$, $P^2 = P = P^T$.

However, the construction of such operator requires the retrieval of aforementioned subspaces. The key thought is that all the ice-free frames IF must have the same projection: $\exists c_0 \forall c \in IF : P(c) = c_0$. To achieve this, the frame c_0 with neither ice nor noise should be chosen by hand. We obtained several candidates for such a frame through visual assessment and peaked the pixel-wise minimum of all of them. Then artifact subspace A is constructed from IF to match orthogonality condition to c_0 at least, and the filtering operator P is constructed after choosing a basis in the subspace containing all the artifacts A :

$$A = \left\{ v - \frac{(v, c_0)}{(c_0, c_0)} c_0 \mid v \in IF \right\}, \quad P(v) = v - \sum_{i=1}^n \frac{(v, e_i)}{(e_i, e_i)} e_i \quad (1)$$

where $\{e_i\}_{i=1}^n$ is a basis in the linear span of A .

Metrics

In our research we utilize two type of metrics. First, we use the common computer vision ones: the mean squared error (MSE) also known as L2-distance; the structural similarity index measure (SSIM), a metric used to assess the human-perceived quality of digital images and videos [16], predominantly used in computer vision; and the multi-scale

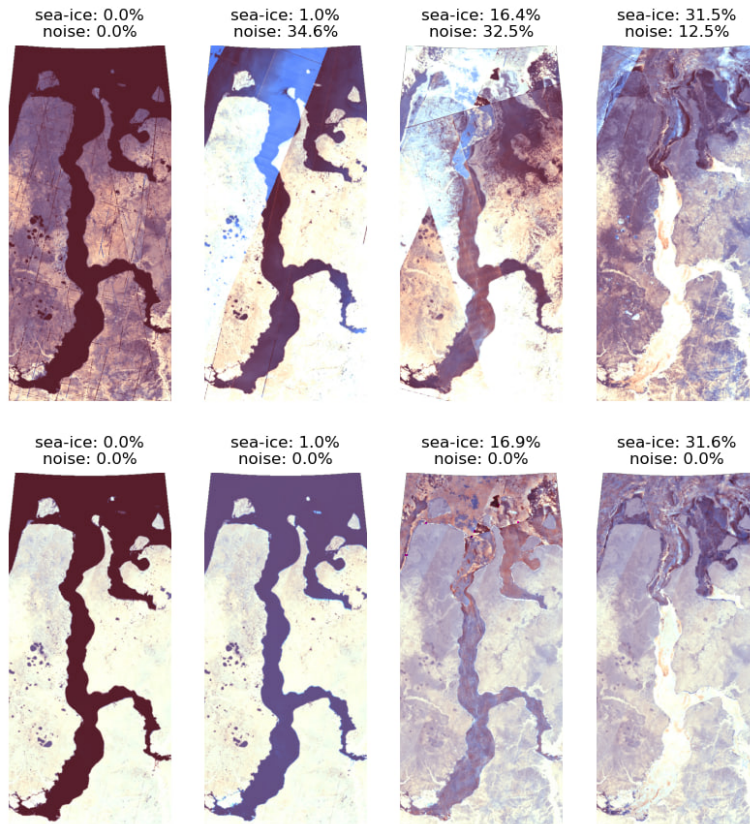


Figure 5: Examples of images before filtration (the first line) and after (the second line). Percentage of noise is a ratio of detected imagery artifacts intensity, percentage of sea-ice is the ratio of residual intensity of variance from noise- and ice-free frame c_0 , that is presented in the upper left corner of the figure. Images are colorized according to [37].

structural similarity index measure (MS-SSIM), which extends the concept of the SSIM by evaluating image quality at various scales [17]. The MS-SSIM approach uses the fact that the human eye perceives picture quality differently across varying resolutions, making it a more comprehensive metric for assessing the perceived quality of digital images and videos. Second, we use a geophysical metric specific for sea ice condition analysis and forecast: the integrated ice edge error at level c (IIEE at c), a metric of similarity between ice sheets, where ice edges are chosen at the certain level of concentration c measured in percents [18]:

$$IIEE@c = \frac{1}{n} \sum_{i=1}^n \frac{1}{S} \sum_{h,w} [(y_i > c) \neq (\hat{y}_i > c)] dS_{hw}, \quad S = \sum_{h,w} dS_{hw} \quad (2)$$

where y_i and \hat{y}_i are linearly normalized into range $[0, 100]$. Usually parameter c is set to 15%, however we can not assume a linear relationship between ice concentration and SAR images, thus we will exploit several values for c .

Video Prediction Models

In this section we describe the investigated in our research models that we reuse or adopt for sea ice forecasting.

Baselines. To determine the relative quality of our models performance, we compare them against two baselines: persistence forecast and linear one. To obtain the parameters of the linear transformation we utilize the same techniques as for deep learning models.

IAM4VP[12] is fully convolutional neural network that leverages the trade-off between temporal-consistency of autoregressive methods and error-independence of non-autoregressive ones via implicit Multi-Input-Single-Output workflow. Like non-autoregressive methods, stacked autoregressive approach uses the same observed sequence to estimate future frames. However, the suggested model uses its own predictions as input, similar to autoregressive methods. As the number of time steps increases, predictions are sequentially stacked in the queue. The architecture is

composed of three main blocks: encoder, predictor and decoder. Encoder and decoder serve to acquire and predict spatial features, while predictor aggregates spatio-temporal information to generate next state. After the iterative process is finished, all generated frames are refined by the last few layers to raise the temporal correlations. The proposed approach both generates consistent predictions and breaks the error-accumulation chain.

DMVFN[13] is a video prediction model leveraging voxel flow estimation to focus on movement and to handle the occlusion effect. DMVFN also incorporates a dynamic routing module that adaptively selects sub-networks based on the input frames, allowing it to handle diverse motion scales efficiently. The model’s architecture includes Multi-scale Voxel Flow Blocks (MVFBs) that capture large motions and iteratively refine voxel flow estimates. DMVFN demonstrates improved efficiency and adaptability, particularly for videos with complex motion patterns and is considered a state-of-the-art deep learning solution for video prediction.

MotionRNN [14] is a model designed for video prediction, specifically addressing the challenge of predicting continuous spatio-temporal dynamics. MotionRNN is a successor of the LSTM-based architectures that also incorporates warp transformation and introduces the concept of breaking down physical motions into transient variation and motion trend. Transient variation represents immediate changes, while the motion trend captures the overall direction or tendency of movements over time. This model is particularly focused on capturing the complex variations within motions that traditional models often overlook, enabling it to adapt to highly dynamic scenarios.

Neural ODE[40] offers a powerful framework for modeling dynamic systems by means of machine learning. The core idea is to model the transformation of data through a continuous dynamic equation in a Cauchy formulation instead of discrete layers used in traditional neural networks. The forward pass is a numerical solution of a parametrized ODE. To train Neural ODEs through backpropagation the gradients can be computed either directly through the dynamic equation using automatic differentiation or more memory-efficiently through the adjoint method. The adjoint method treats gradients as solutions of a reverse-time differential equations, integrating it backwards in time.

Vid-ODE [15] represents Neural ODE in a latent space on motion-vector dynamics (optical flow prediction) with a warp-correction mechanism. The main idea of Vid-ODE lies in the parameterizing visual attributes such as pixels position by utilizing differential equations. The input frames are transformed to latent states by convolutional encoder block, then they are assimilated into an evolving state by the GRU cell, and Neural ODE models its inner dynamics. The predicted state is transformed by convolutional decoder into pixels relative shifts and correction features that are used to correct warping impurities and model color and brightness variation. Finally, all channels are fused into the output sequence. This iterative process ensures smooth transitions between generated frames.

UNet [41], is an image-to-image convolutional neural network (CNN) which includes a contracting path (encoder) for capturing context and an expansive path (decoder) for precise localization for the output. The decoder path involves upsampling of the feature maps and concatenates them with the corresponding feature maps from the encoder path. Originally designed for the biomedical image segmentation, UNet has been adapted for different geophysical fields forecasts such as: coastal sea elements [20], precipitation [42, 43], and sea ice concentration [21, 22]. These advancements motivated us to apply the UNet architecture in our research as well.

Model	Regime	Input size	GFLOPS	Params
Persistence	-	-	-	0
Linear	SISO	7	33	1.06 K
DMVFN	MISO	7	198	3.56 M
IAM4VP	Implicit MISO	10	76	27.8 M
Neural ODE	SISO	7	200 ± 100	18.53 K
MotionRNN	SISO	7	10610	6.84 M
Vid-ODE	SISO	7	480 ± 150	469 K
UNet	MIMO	7	559	31.10 M
rUNet	SISO	7	4780	31.04 M

Table 2: Model configurations. Regime abbreviations are constructed as follows: SI stands for Single-Input, MI — Multi-Input, SO — Single-Output, and MO — Multi-Output, based on sequence lengths: Single-Input models acquire input iteratively, Multi-Input — at once; Single-Output models are autoregressive predictors; Multi-Output — non-autoregressive. Computational costs for each model (in GFLOPS) are provided per one input sequence. ODE-based models use adaptive solvers; the adaptive time step leads to varying GFLOPS; its standard deviation is provided.

Implementation and training

All models are implemented in PyTorch and trained from scratch with AdamW optimizer [44]. The loss function is a combination of MSE and SSIM losses:

$$L = \text{MSE} - 0.2 \cdot \text{SSIM} \quad (3)$$

The initial learning rate is set to 10^{-3} and exponentially decreasing with factor $\gamma = 0.99$. The batch size is set to 32. Models are trained until either convergence of validation metrics or the overfitting begins (early-stopping). Models with the best validation score are evaluated after on the test-subset.

To mitigate bias on missed parts of the input, normalization layers were removed from encoders of Single-Input models. While training Neural ODE and Vid-ODE models, naive implementations of the adjoint method might suffer from inaccuracy in reverse-time trajectory computation, therefore in our work we have used specific implementation called MALI [45] that guarantees accuracy in gradient estimation. The overall models configurations are provided in Table 2.

Augmentations

To prevent overfitting and improve generalization ability we utilize geometrical augmentations: random horizontal flips with a probability of 0.5 and uniformly sampled random rotations with angles in range $[-10^\circ, 10^\circ]$ with the corresponding rotation of wind and sea-currents field. To leverage the imbalance of missing values depicted at Figure 4 we utilized frameout augmentation. Up to three random frames in the input sequence are cut out until the concentration of missing values reaches the level of the test subset (70%).

Uncertainty-awareness

Estimating uncertainty in data-driven weather forecasting models is crucial for better model interpretation and decision-making. If the uncertainty estimation is well-calibrated, the reliable predictions are characterized by high confidence. On the other hand, low confidence means the prediction can not be trusted. In such cases one could replace it with a simple baseline or a more robust model. Following this principle, automatized pipelines of confidence-based model selection can be designed [46, 47, 48, 49]. The mechanism is as follows: the expert model makes a prediction, its uncertainty is estimated; if the uncertainty exceeds the preset threshold, the prediction is replaced by more stable baseline. In our work the threshold is selected on the validation subset. This helps to exclude unreliable forecasts and enhances the overall performance of the forecasting system.

In the realm of deep learning, uncertainty estimation is commonly implemented in the form of learning output probability distribution, therefore it is integrated into the model architecture [46]. This approach often requires a large amount of data and specialized training procedures, leading to issues with calibration for the limited amount of data. Deep ensemble methods offer a solution to this problem by combining multiple models to improve overall performance and uncertainty estimation [46].

On the other hand, traditional weather and climate models estimate uncertainty as the spread of an ensemble, constructed by the model inputs perturbations[50]. The ensemble spread is defined as a standard deviation of predictions. Previous research [51] showed that, when using neural networks, ensembles of models with similar architectures (homogeneous) provide similar results. Models weights in the ensemble have to be perturbed with retraining, dropout, etc. Moreover, there are premises that an ensemble of diverse architectures (heterogeneous) might provide better uncertainty estimation [52].

In our research we construct both homogeneous and heterogeneous ensembles and compare their spread as a predictor for the uncertainty estimation for the model selection mechanism. The suggested pipeline does not impose additional costs as all the models do not need to be modified or retrained.

Results

Forecasting

While designing the experiments, we focused on evaluating the performance and stability of various forecasting models. Our results reveal a trade-off between achieving high computer vision metrics and maintaining forecast stability — while some models excel in certain metrics, their forecasts can be less consistent. However, we found that an ensemble of four high-performing models with diverse architectures — namely MotionRNN, Vid-ODE, UNet, and rUNet — offers robust uncertainty estimation. The most significant improvement over the baseline across nearly all metrics was achieved using a confidence-based model selection pipeline, which utilized an rUNet backbone, an autoregressive UNet, and DMVFN as a robust alternative.

Model	MSE	1 - SSIM ($\times 10^{-3}$)	1 - MS-SSIM	IIEE@15	IIEE@30	IIEE@50	IIEE@75 ($\times 10^{-2}$)
Persistence	11.2	9.8	5.6	11.5	10.4	11.0	7.3
Linear	9.8	9.1	5.2	14.0	9.6	11.1	7.7
DMVFN	10.0	8.8	5.1	11.7	10.2	10.8	6.9
IAM4VP	8.7	10.5	5.5	14.7	10.6	11.0	7.1
Neural ODE	8.3	9.3	4.9	12.1	10.1	10.7	6.2
MotionRNN	7.3	9.0	4.7	11.4	9.3	9.9	5.9
Vid-ODE	7.5	8.7	4.7	12.1	9.2	9.7	5.7
UNet	7.7	8.2	4.6	12.1	9.3	9.6	6.0
rUNet	6.8\pm0.2	8.3 \pm 0.2	4.5\pm0.1	10.0\pm1.1	9.0\pm0.3	9.2\pm0.2	5.3\pm0.2

Table 3: Summary of the test metrics (lower is better) for models with confidence-based mixture with DMVFN as a robust model; the confidence is estimated by the ensemble spread of predictions from MotionRNN, Vid-ODE, UNet, and rUNet models. The standard deviation for the best model (rUNet) is estimated by training with three random initializations.

Ensemble	MSE	1 - SSIM ($\times 10^{-3}$)	1 - MS-SSIM	IIEE@15	IIEE@30	IIEE@50	IIEE@75 ($\times 10^{-2}$)
rUNet x3	6.7	8.3	4.5	10.0	8.9	9.1	5.3
Best 4	6.6	8.2	4.4	11.2	8.7	9.3	5.2

Table 4: Summary of the test metrics for ensembles. Confidence-based mixture with DMVFN is utilized. “rUNet x3” stands for mean forecast of three retrained versions of rUNet. “Best 4” stands for mean prediction from MotionRNN, Vid-ODE, UNet, and rUNet models.

A summary of the metrics evaluated on the test subset for all trained models with confidence-based model selection is presented in Table 3. Figure 6 shows detailed improvements over the baseline, broken down by month and lead time. Examples of predictions are provided in Figure 11. Using the mean of ensembles instead of model selection yields only a marginal improvement in the final metrics, as shown in Table 4.

Following the Grigoryev’s work[21], models trained to produce 3-day forecasts were also tested with 10-day outputs without any additional fine-tuning. The results are presented in Figure 7. Linear and ODE-based models accumulate errors exponentially, degrading over persistence after the 5-th day. Other models errors increase linearly over time, providing stable improvement over persistence, except IAM4VP which manages to overcome all other models after the 7-th day of the forecast.

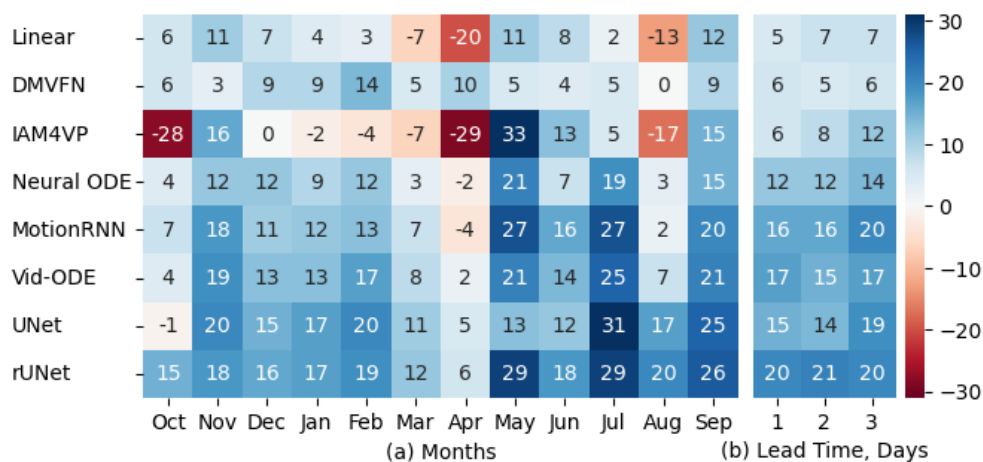


Figure 6: The RMSE percentage improvement over persistence baseline for each month (a), and for each lead time in days (b), over the test subset. The colormap is shared.

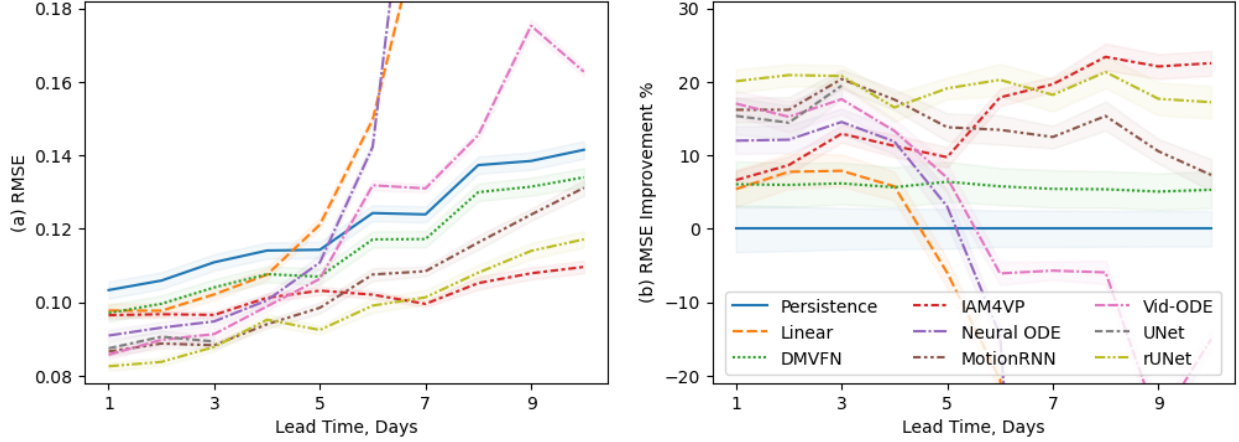


Figure 7: (a) RMSE and (b) its percentage improvement over persistence baseline for each extended lead time in days over the test subset.

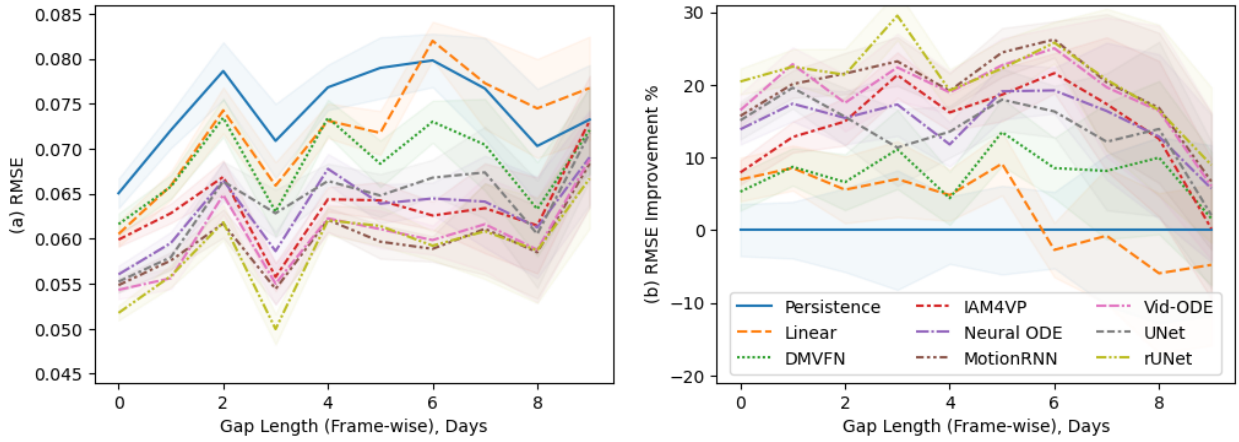


Figure 8: (a) RMSE and (b) its percentage improvement over persistence baseline in dependence of preceding SAR gap length.

Due to the irregular intervals at which satellites capture the target region, a strong correlation between model performance and the length of gaps between valid images is expected. This relationship is illustrated in Figure 8, where RMSE generally increases linearly until the gap length surpasses the models' input size. Once this threshold (7 days) is exceeded, the RMSE approaches that of the persistence baseline.

Gap filling

The developed pipeline is particularly useful for filling gaps in SAR images, a common issue in satellite data. Building on the approach proposed by Appel[31], this gap-filling process can be effectively performed as a 1-day forecast. To improve accuracy, we combine forward and backward forecasts, denoted as y_F and y_B , respectively. By incorporating the uncertainty estimates of these forecasts, σ_F and σ_B , we can weight them appropriately and calculate an overall confidence using a harmonic mean:

$$y = \frac{\sigma_B}{\sigma_F + \sigma_B} y_F + \frac{\sigma_F}{\sigma_F + \sigma_B} y_B, \quad \sigma = \frac{2\sigma_F\sigma_B}{\sigma_F + \sigma_B} \quad (4)$$

A key advantage of this approach is that it does not require retraining the models. We evaluated the performance of this gap-filling method using a leave-one-out cross-validation technique[53]. For comparison, we also tested the pretrained AdaCoF model[54], which is one of the state-of-the-art models for video interpolation. As shown in Table 5, our pipeline achieved a strong R^2 value of 87.7%. This is consistent with similar R^2 values reported in the literature[30, 31] for gap-filling in satellite imagery under similar conditions, such as missing swaths up to 500 km wide and 1 kilometer resolution.

Model	MSE	1 - SSIM	1 - MS-SSIM	IIEE@15	IIEE@30	IIEE@50	IIEE@75
		$(\times 10^{-3})$					
AdaCoF	7.3	8.3	4.5	8.0	7.9	9.2	6.0
Forward	6.5	8.1	4.4	8.6	8.5	9.2	5.3
Forward+Backward	6.0	7.6	4.1	9.1	7.7	8.7	5.7

Table 5: Summary of gap filling metrics obtained during a leave-one-out validation. Confidence-based mixture of rUNet and DMVFN is utilized for forward and backward forecasts, where the “Forward+Backward” is a confidence-based weighted mean. The input channels related to wind and currents are reversed for the backward run. The best metric values in each column are highlighted in bold.

Discussion

This research addresses the critical challenge of short-term regional sea ice forecasting, exploring a variety of approaches to improve prediction accuracy and reliability. Among the methods investigated, modern deep learning models for video prediction were tested for their potential in forecasting sea ice dynamics. However, the performance of these models is constrained by several factors, including the scarcity of high-resolution data, the complex physical processes governing sea ice behavior, the stochastic nature of daily ice dynamics, and the discontinuities present in ice sheet structures.

UNet-based models deliver the best individual results, whereas state-of-the-art video prediction models struggle to surpass baseline performance, though they do offer varying levels of stability. It could be argued that the DMVFN model fails to accurately reproduce sea ice thermodynamics due to its architectural limitations, which, paradoxically, contribute to more stable forecasts. On the other hand, IAM4VP, while efficient at modeling different dynamics with minimal computational cost, produces the most unstable predictions, likely due to the lack of sufficient training data.

Advanced use of confidence-based model selection can further enhance the metrics. The ensemble spread of heterogeneous architectures provides accurate uncertainty estimation for the forecasted fields. Although the model-selection mechanism reduces the final spread-error correlation, the total variance in model error can still be explained up to 87% by accounting for the sea ice concentration and its rate of change (see Figure 9).

A fundamental challenge with state-of-the-art machine learning models is their inability to replicate the complex mechanics of sea ice in coastal regions. The poor performance in capturing fine-scale ice mechanics is not unique to any one method but is a common issue across various approaches at the target resolution. For instance, neither modern sea ice motion vectors [10, 55] nor optical flow estimation methods [56, 57, 58] are well-suited for high-resolution ice velocity estimation. This degradation in quality when transitioning to higher resolutions is illustrated in Figure 10. Moreover, deep learning methods for optical flow estimation may be overfitted on conventional images and lack the generalization needed for sea ice SAR imagery. Consequently, motion information is scarcely useful for predictions in the region of interest. We argue that improving the quality of fine-grained sea ice motion vectors is a crucial area for future research.

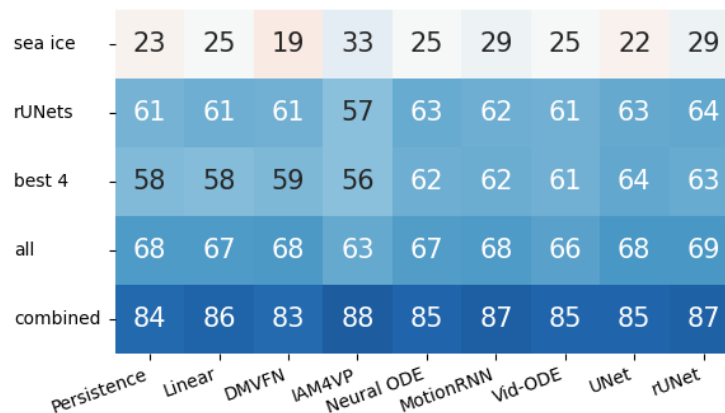


Figure 9: Correlation (in percents) between models RMSE (with confidence-based model selection) and several features: sea ice concentration, ensemble spread, and their learned linear combination.

Resolution:	1 km	2 km	4 km	8 km	16 km	32 km
Persistence	7.0	7.2	7.2	7.4	7.1	7.5
Glorys Operative	8.6	8.8	8.2	8.4	6.9	5.6
AMSR JAXA SIM-R	7.1	6.9	6.6	6.4	6.3	5.8
Farneback	6.7	6.6	6.4	6.4	6.5	5.9
CrocoFlow	6.8	6.7	6.5	6.4	6.5	5.9
PWC-Net	6.9	6.8	6.5	6.4	7.0	8.2

Figure 10: Mean Squared Error (MSE) ($\times 10^{-3}$) between next-day images and previous-day images, warped using estimated flow from various sources. These sources include the GLORYS Operative model (25 km resolution), AMSR JAXA SIM-R (50 km resolution), and several Optical Flow models, such as the algorithmic Farneback method and state-of-the-art neural networks. The best MSE values for each resolution are highlighted in bold.

Conclusions

In this research article, we address the challenge of predicting ice conditions in the Gulf of Ob, a region characterized by complex ice formation dynamics influenced by the interaction of saline water and freshwater. We explore the potential of machine learning methods as an alternative to traditional numerical sea ice models, aiming to improve forecasting accuracy and efficiency.

Our key findings reveal that even modern state-of-the-art machine learning models can not achieve sufficient forecasting performance solely. Furthermore, domain-aware data preprocessing and augmentations are essential to train deep learning models for this task. All models struggle due to lack of training data, long gaps in it and complex sea ice dynamics, leading to tricky fidelity-stability trade-off. Although usage of ensembles cannot significantly improve average models performance, it helps to eliminate high errors due to outliers in data, especially in spring season thus increasing overall system reliability. In addition, we observed high spread-error correlation for both homogeneous and heterogeneous ensembles, therefore the ensemble spread can serve as reliable uncertainty estimation. To overcome the aforementioned trade-off we construct the confidence-based model selection pipeline, that provides both stable and explainable forecasts while improving general performance. The mixture of the rUNet and DMVFN architectures provides the best computer vision and geophysical metrics.

Finally, we discuss the limitations of video prediction models when applied to sea ice forecasting. The unusual domain of homogeneous ice sheets, sophisticated physics, and chaotic dynamics on a sparse daily timescale pose significant challenges. Sea ice motion vectors and optical flow estimation methods also have limitations in this specific domain due to the lack of suitable data and the unique characteristics of ice sheets.

Future research directions include exploring the approaches for retrieving the high-resolution ice motion vectors and improving optical flow estimation methods for ice sheets. Developing models that can effectively capture the dynamics of ice formation and melting is crucial. Additionally, addressing the limitations of current approaches through more advanced architectures and techniques can also be beneficial. Further advancements in sea ice forecasting will not only improve maritime navigation safety but also deepen our understanding of complex sea ice dynamics.

Funding

The work was supported by the Analytical center under the RF Government (subsidy agreement 000000D730321P5Q0002, Grant No. 70-2021-00145 02.11.2021).

Author contributions statement

S.A., T.G. and V.V. conceived the ideas, A.N. and T.G. curated the data, S.A. conducted experiments and provided visualizations, S.A., T.G. and V.V. analysed the results. S.A. and A.N. wrote the first draft, all authors reviewed and edited the manuscript.

Competing interests

The authors declare no competing interests.

Availability

The code and processed data will be published when the manuscript is reviewed.

References

- [1] R Kwok. Arctic sea ice thickness, volume, and multiyear ice coverage: losses and coupled variability (1958–2018). *Environmental Research Letters*, 13(10):105005, 2018.
- [2] Aleksi Nummelin, Mehmet Ilicak, Camille Li, and Lars H. Smedsrud. Consequences of future increased arctic runoff on arctic ocean stratification, circulation, and sea ice cover. *Journal of Geophysical Research: Oceans*, 121(1):617–637, 2016.
- [3] Rosemary Eastwood, R. Macdonald, Jens Ehn, Joel Heath, L. Arragutainaq, Paul Myers, D. Barber, and Zou Zou Kuzyk. Role of river runoff and sea ice brine rejection in controlling stratification throughout winter in southeast hudson bay. *Estuaries and Coasts*, 43, 03 2020.
- [4] Ming Li, Ren Zhang, and Kefeng Liu. Machine learning incorporated with causal analysis for short-term prediction of sea ice. *Frontiers in Marine Science*, 8, may 2021.
- [5] James E. Overland and Carol H. Pease. Modeling ice dynamics of coastal seas. *Journal of Geophysical Research: Oceans*, 93(C12):15619–15637, 1988.
- [6] John Wallace Weatherly and John E. Walsh. The effects of precipitation and river runoff in a coupled ice-ocean model of the arctic. *Climate Dynamics*, 12:785–798, 1996.
- [7] Alexander Osadchiev, Olga Konovalova, and Alexandra Gordey. Water exchange between the gulf of ob and the kara sea during ice-free seasons: The roles of river discharge and wind forcing. *Frontiers in Marine Science*, 8, dec 2021.
- [8] Copernicus sentinel data 2024, processed by esa.
- [9] Weather and Climate. Weather archive. <http://www.pogodaiklimat.ru>.
- [10] European union-copernicus marine service. glorys12v1.
- [11] Ruibo Ming, Zhewei Huang, Zhuoxuan Ju, Jianming Hu, Lihui Peng, and Shuchang Zhou. A survey on video prediction: From deterministic to generative approaches, 2024.
- [12] Min-seok Seo, Hakjin Lee, Doyi Kim, and Junghoon Seo. Implicit stacked autoregressive model for video prediction. *ArXiv*, 2023.
- [13] Xiaotao Hu, Zhewei Huang, Ailin Huang, Jun Xu, and Shuchang Zhou. A dynamic multi-scale voxel flow network for video prediction. In *2023 IEEE/CVF Conference on Computer Vision and Pattern Recognition (CVPR)*, pages 6121–6131, 2023.
- [14] Haixu Wu, Zhiyu Yao, Jianmin Wang, and Mingsheng Long. Motionrnn: A flexible model for video prediction with spacetime-varying motions. In *2021 IEEE/CVF Conference on Computer Vision and Pattern Recognition (CVPR)*. Ieee, jun 2021.
- [15] Sunghyun Park, Kangyeol Kim, Junsoo Lee, Jaegul Choo, Joonseok Lee, Sookyung Kim, and Edward Choi. Vid-ode: Continuous-time video generation with neural ordinary differential equation. *Proceedings of the AAAI Conference on Artificial Intelligence*, 35(3):2412–2422, may 2021.
- [16] Z. Wang, A.C. Bovik, H.R. Sheikh, and E.P. Simoncelli. Image quality assessment: From error visibility to structural similarity. *IEEE Transactions on Image Processing*, 13(4):600–612, apr 2004.
- [17] Z. Wang, E.P. Simoncelli, and A.C. Bovik. Multiscale structural similarity for image quality assessment. In *The Thirty-Seventh Asilomar Conference on Signals, Systems & Computers, 2003*, ACSSC-03. IEEE, 2003.
- [18] H. F. Goessling, S. Tietsche, J. J. Day, E. Hawkins, and T. Jung. Predictability of the arctic sea ice edge. *Geophysical Research Letters*, 43(4):1642–1650, 2016.
- [19] Junhwa Chi and Hyun-choel Kim. Prediction of arctic sea ice concentration using a fully data driven deep neural network. *Remote Sensing*, 9(12):1305, dec 2017.
- [20] Jesús García Fernández, Ismail Alaoui Abdellaoui, and Siamak Mehrkanoon. Deep coastal sea elements forecasting using unet-based models. *Knowledge-Based Systems*, 252:109445, sep 2022.
- [21] Timofey Grigoryev, Polina Verezhenskaya, Mikhail Krinitskiy, Nikita Anikin, Alexander Gavrikov, Ilya Trofimov, Nikita Balabin, Aleksei Shpilman, Andrei Eremchenko, Sergey Gulev, Evgeny Burnaev, and Vladimir Vanovskiy. Data-driven short-term daily operational sea ice regional forecasting. *Remote Sensing*, 14(22), 2022.

- [22] A. F. Kvanum, C. Palerme, M. Müller, J. Rabault, and N. Hughes. Developing a deep learning forecasting system for short-term and high-resolution prediction of sea ice concentration. *EGUsphere*, pages 1–26, 2024.
- [23] Mary Ruth Keller, Christine Piatko, Mary Versa Clemens-Sewall, Rebecca Eager, Kevin Foster, Christopher Gifford, Derek Rollend, and Jennifer Sleeman. Short-term (7 day) beaufort sea ice extent forecasting with deep learning. *Artificial Intelligence for the Earth Systems*, 2(4):e220070, 2023.
- [24] Sean Horvath, Julienne Stroeve, Balaji Rajagopalan, and William Kleiber. A bayesian logistic regression for probabilistic forecasts of the minimum september arctic sea ice cover. *Earth and Space Science*, 7(10), 2020.
- [25] Tom R Andersson, J Scott Hosking, María Pérez-Ortiz, Brooks Paige, Andrew Elliott, Chris Russell, Stephen Law, Daniel C Jones, Jeremy Wilkinson, Tony Phillips, et al. Seasonal arctic sea ice forecasting with probabilistic deep learning. *Nature Communications*, 12(1):5124, Aug 2021.
- [26] Da Wu, Xiao Lang, Wengang Mao, Di Zhang, Jinfen Zhang, and Rong Liu. Vae based non-autoregressive transformer model for sea ice concentration forecast. *International Ocean and Polar Engineering Conference*, 06 2022.
- [27] Asadi Nazanin. *Data-driven Regularization and Uncertainty Estimation to Improve Sea Ice Data Assimilation*. PhD thesis, University of Waterloo, 2019.
- [28] Xinwei Chen, Ray Valencia, Armina Soleymani, and K. Andrea Scott. Predicting sea ice concentration with uncertainty quantification using passive microwave and reanalysis data: A case study in baffin bay. *IEEE Transactions on Geoscience and Remote Sensing*, 61:1–13, 2023.
- [29] Manali Desai and Amit Ganatra. Survey on gap filling in satellite images and inpainting algorithm. *International Journal of Computer Theory and Engineering*, page 341–345, 2012.
- [30] Daniel J. Weiss, Peter M. Atkinson, Samir Bhatt, Bonnie Mappin, Simon I. Hay, and Peter W. Gething. An effective approach for gap-filling continental scale remotely sensed time-series. *ISPRS Journal of Photogrammetry and Remote Sensing*, 98:106–118, dec 2014.
- [31] Marius Appel. Efficient data-driven gap filling of satellite image time series using deep neural networks with partial convolutions. *Artificial Intelligence for the Earth Systems*, 3(2), apr 2024.
- [32] S. A. Lapin, E. L. Mazo, and P. N. Makkaveev. Integrated research on the gulf of ob (july to october 2010). *Oceanology*, 51(4):711–715, aug 2011.
- [33] M. V. Tretiakov and A. I. Shiklomanov. Assessment of influences of anthropogenic and climatic changes in the drainage basin on hydrological processes in the gulf of ob. *Water Resources*, 49(5):820–835, sep 2022.
- [34] V. V. Tikhonov, A. N. Romanov, I. V. Khvostov, T. A. Alekseeva, A. I. Sinitskiy, M. V. Tikhonova, E. A. Sharkov, and N. Yu. Komarova. Analysis of the hydrological regime of the gulf of ob in the freezing period using smos data. *Rossiyskaya Arktika*, 2022.
- [35] Grace Wahba. *Spline Models for Observational Data*. Society for Industrial and Applied Mathematics, jan 1990.
- [36] Valentin Ludwig, Gunnar Spreen, and Leif Toudal Pedersen. Evaluation of a new merged sea-ice concentration dataset at 1 km resolution from thermal infrared and passive microwave satellite data in the arctic. *Remote Sensing*, 12(19), 2020.
- [37] Sentinel hub. <https://custom-scripts.sentinel-hub.com/sentinel-1/sar-ice/>.
- [38] Zheng Chang, Xinfeng Zhang, Shanshe Wang, Siwei Ma, and Wen Gao. Strpm: A spatiotemporal residual predictive model for high-resolution video prediction. *arXiv preprint arXiv:2203.16084*, 2022.
- [39] Prabhishkek Singh, Manoj Diwakar, Achyut Shankar, Raj Shree, and Manoj Kumar. A review on sar image and its despeckling. *Archives of Computational Methods in Engineering*, 28(7):4633–4653, 2021.
- [40] Ricky T. Q. Chen, Yulia Rubanova, Jesse Bettencourt, and David K Duvenaud. Neural ordinary differential equations. In S. Bengio, H. Wallach, H. Larochelle, K. Grauman, N. Cesa-Bianchi, and R. Garnett, editors, *Advances in Neural Information Processing Systems*, volume 31. Curran Associates, Inc., 2018.
- [41] Olaf Ronneberger, Philipp Fischer, and Thomas Brox. *U-Net: Convolutional Networks for Biomedical Image Segmentation*, page 234–241. Springer International Publishing, 2015.
- [42] Christos Kaparakis and Siamak Mehrkanoon. Wf-unet: Weather fusion unet for precipitation nowcasting, 2023.
- [43] Kevin Trebing, Tomasz Stanczyk, and Siamak Mehrkanoon. Smaat-unet: Precipitation nowcasting using a small attention-unet architecture. *Pattern Recognition Letters*, 145:178–186, may 2021.

- [44] Adam Paszke, Sam Gross, Francisco Massa, Adam Lerer, James Bradbury, Gregory Chanan, Trevor Killeen, Zeming Lin, Natalia Gimelshein, Luca Antiga, Alban Desmaison, Andreas Kopf, Edward Yang, Zachary DeVito, Martin Raison, Alykhan Tejani, Sasank Chilamkurthy, Benoit Steiner, Lu Fang, Junjie Bai, and Soumith Chintala. Pytorch: An imperative style, high-performance deep learning library. In H. Wallach, H. Larochelle, A. Beygelzimer, F. d'Alché-Buc, E. Fox, and R. Garnett, editors, *Advances in Neural Information Processing Systems*, volume 32. Curran Associates, Inc., 2019.
- [45] Juntang Zhuang, Nicha C Dvornek, Sekhar Tatikonda, and James Duncan. {MALI}: A memory efficient and reverse accurate integrator for neural {ode}s. In *International Conference on Learning Representations*, 2021.
- [46] Balaji Lakshminarayanan, Alexander Pritzel, and Charles Blundell. Simple and scalable predictive uncertainty estimation using deep ensembles. In I. Guyon, U. Von Luxburg, S. Bengio, H. Wallach, R. Fergus, S. Vishwanathan, and R. Garnett, editors, *Advances in Neural Information Processing Systems*, volume 30. Curran Associates, Inc., 2017.
- [47] Annie Chen, Yoonho Lee, Amrith Setlur, Sergey Levine, and Chelsea Finn. Confidence-based model selection: When to take shortcuts for subpopulation shifts, 06 2023.
- [48] Hanqing Zeng, Hanjia Lyu, Diyi Hu, Yinglong Xia, and Jiebo Luo. Mixture of weak and strong experts on graphs, 2023.
- [49] Yuchang Jiang, Vivien Sainte Fare Garnot, Konrad Schindler, and Jan Dirk Wegner. Mixture of experts with uncertainty voting for imbalanced deep regression problems, 2023.
- [50] Eric P. Grimit and Clifford F. Mass. Measuring the ensemble spread–error relationship with a probabilistic approach: Stochastic ensemble results. *Monthly Weather Review*, 135(1):203 – 221, 2007.
- [51] Sebastian Scher and Gabriele Messori. Ensemble methods for neural network-based weather forecasts. *Journal of Advances in Modeling Earth Systems*, 13(2), 2021.
- [52] Shehryar Zaidi, Arber Zela, Thomas Elsken, Chris Holmes, Frank Hutter, and Yee Whye Teh. Neural ensemble search for uncertainty estimation and dataset shift, 2022.
- [53] Ron Kohavi. A study of cross-validation and bootstrap for accuracy estimation and model selection. In *Proceedings of the 14th International Joint Conference on Artificial Intelligence - Volume 2, IJCAI'95*, page 1137–1143, San Francisco, CA, USA, 1995. Morgan Kaufmann Publishers Inc.
- [54] Hyeongmin Lee, Taeoh Kim, Tae-young Chung, Daehyun Pak, Yuseok Ban, and Sangyoun Lee. Adacof: Adaptive collaboration of flows for video frame interpolation. In *2020 IEEE/CVF Conference on Computer Vision and Pattern Recognition (CVPR)*. Ieee, jun 2020.
- [55] Kimura Noriaki, Nishimura Akira, Tanaka Yohei, and Yamaguchi Hajime. Influence of winter sea-ice motion on summer ice cover in the arctic. *Polar Research*, 32, 2013.
- [56] Gunnar Farneback. Two-frame motion estimation based on polynomial expansion. In Josef Bigun and Tomas Gustavsson, editors, *Image Analysis*, pages 363–370, Berlin, Heidelberg, 2003. Springer Berlin Heidelberg.
- [57] Philippe Weinzaepfel, Thomas Lucas, Vincent Leroy, Yohann Cabon, Vaibhav Arora, Romain Brégier, Gabriela Csurka, Leonid Antsfeld, Boris Chidlovskii, and Jérôme Revaud. Croco v2: Improved cross-view completion pre-training for stereo matching and optical flow. In *ICCV*, 2023.
- [58] Deqing Sun, Xiaodong Yang, Ming-Yu Liu, and Jan Kautz. PWC-Net: CNNs for optical flow using pyramid, warping, and cost volume. In *CVPR*, 2018.

Appendix

Ablation Study

This section contains ablation studies for crucial parts of training and prediction pipelines: filtration of SAR-imagery artifacts (Table 6), proper augmentations to leverage unbalance and lack of data (Table 7), and the usage of confidence-based model selection and ensembles (Tables 8, 9).

Ensembles usually provide minor improvements except for IIEE@15 metric. However, confidence based model selection suppresses the advantages of ensembles. The usage of model selection (depicted at Table 3) increases MSE and IIEE@75 by 12%.

Model	MSE	1 - SSIM		IIEE@15 IIEE@30 IIEE@50 IIEE@75			
		$(\times 10^{-3})$		$(\times 10^{-2})$			
Persistence	18.5	9.6	6.8	17.3	12.5	10.2	8.5
Linear	15.7	8.9	6.2	17.6	12.9	10.0	8.4
DMVFN	16.7	8.5	6.2	17.2	12.4	9.9	8.1
IAM4VP	16.8	9.7	6.6	18.5	15.5	11.5	10.4
Neural ODE	13.7	8.5	5.8	17.0	12.4	9.9	7.8
MotionRNN	12.7	8.1	5.4	16.2	11.9	9.2	7.6
Vid-ODE	12.2	7.8	5.4	16.5	11.4	8.7	7.1
UNet	13.0	7.6	5.4	15.7	11.4	9.1	7.4
rUNet	13.6	7.8	5.5	15.7	12.0	9.3	7.6

Table 6: Summary of the metrics obtained by testing individual models without data preprocessing. Raw data have high noise-to-signal ratio due to thermal artifacts. These artifacts simultaneously provide huge bias in metrics and corrupt loss function making the models learn filtration and smoothing rather than forecasting sea ice dynamics.

Augmen- tation	MSE	1 - SSIM		IIEE@15 IIEE@30 IIEE@50 IIEE@75			
		$(\times 10^{-3})$		$(\times 10^{-2})$			
None	8.9	9.2	4.9	11.9	9.4	10.8	7.0
Geometric	8.7	9.0	4.8	12.9	10.4	10.9	6.6
Physical	7.8	8.4	4.6	10.1	9.1	10.0	6.1
Proposed	7.6	8.3	4.6	10.0	9.0	9.8	6.0

Table 7: Ablation studies for the augmentations for the best performing model (rUNet). Geometric augmentations are shifts and rotations (treating input as an image). The physical augmentations are modifications of geometrical ones with corresponding transform (rotations and flips) of physical fields (currents and winds). “Proposed” states for superposition of Physical and Frameout augmentations.

Model	MSE	1 - SSIM		IIEE@15 IIEE@30 IIEE@50 IIEE@75			
		$(\times 10^{-3})$		$(\times 10^{-2})$			
Persistence	11.2	9.8	5.6	11.5	10.4	11.0	7.3
Linear	9.9	9.1	5.2	14.2	9.6	11.0	8.0
DMVFN	10.0	8.8	5.1	11.7	10.2	10.8	6.9
IAM4VP	9.5	10.6	5.6	14.7	10.6	11.4	8.1
Neural ODE	8.6	9.3	4.9	12.1	10.1	10.7	6.8
MotionRNN	8.0	9.0	4.7	11.4	9.3	10.3	6.5
Vid-ODE	7.7	8.6	4.7	12.2	9.2	9.6	6.0
UNet	8.3	8.2	4.6	12.1	9.5	9.9	6.5
rUNet	7.6	8.3	4.6	10.0	9.0	9.8	6.0

Table 8: Summary of test metrics for individual models with proposed preprocessing and augmentations.

Ensemble	MSE	1 - SSIM		IIEE@15	IIEE@30	IIEE@50	IIEE@75
		$(\times 10^{-3})$					
rUNet x3	7.1	8.3	4.5	11.2	8.8	9.2	6.1
Best 4	7.1	8.2	4.4	11.2	8.7	9.4	6.1

Table 9: Summary of test metrics for ensembles. “rUNet x3” stands for mean forecast of 3 retrained versions of rUNet. “Best 4” stands for mean of MotionRNN, Vid-ODE, UNet, and rUNet predictions.

Forecast example

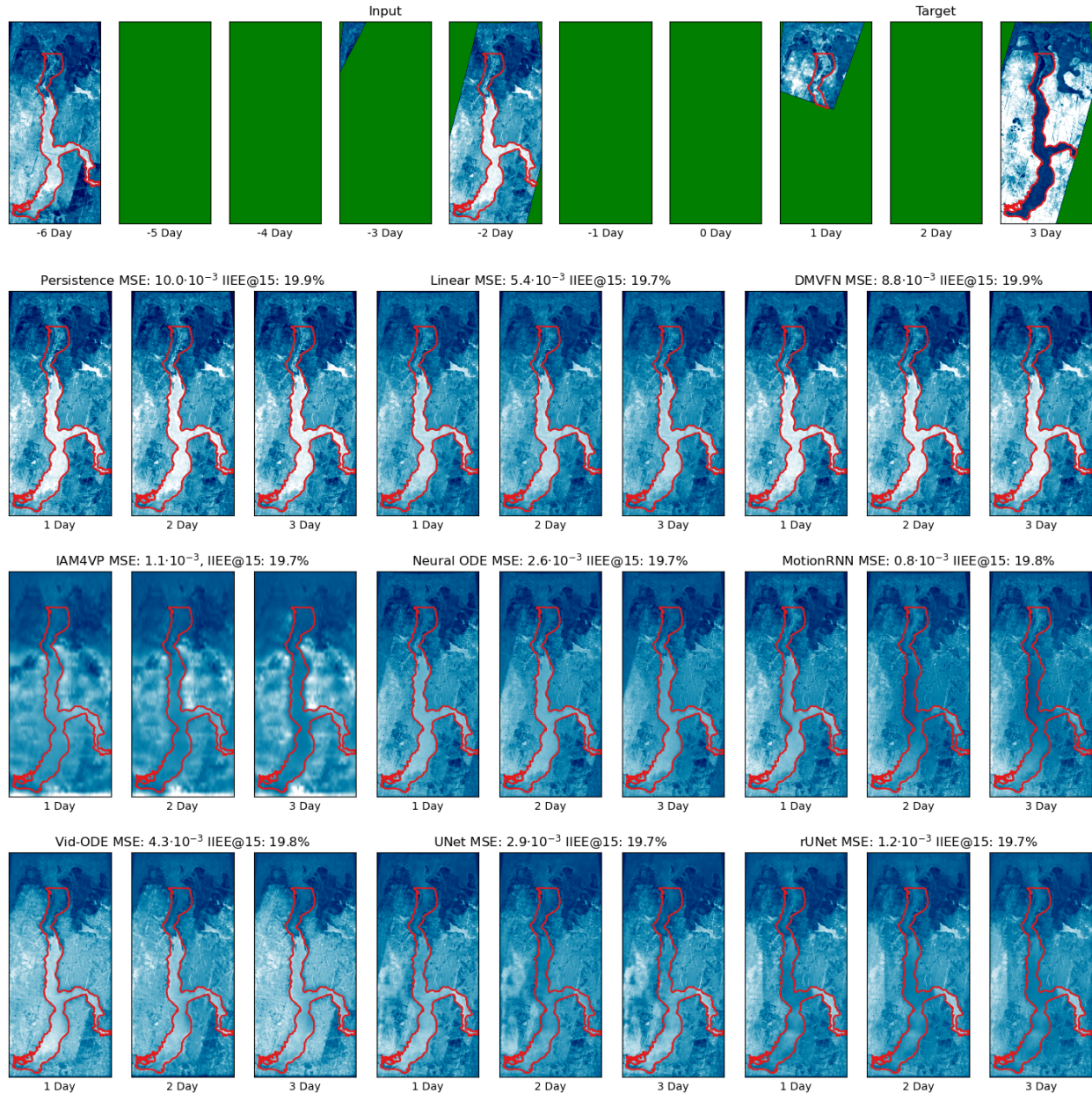


Figure 11: The example of forecasts. Timestamps represent shifts from the 25-05-2023. The target region is outlined with a red line. The missed data in an input and a target sequences is represented by green color.